Searching for Dark Matter Annihilation from Milky Way Dwarf Spheroidal Galaxies with Six Years of Fermi-LAT Data

M. Ackermann,[1] A. Albert,[2] B. Anderson,[3,4,*] W. B. Atwood,[5] L. Baldini,[6,2] G. Barbiellini,[7,8] D. Bastieri,[9,10] K. Bechtol,[11] R. Bellazzini,[12] E. Bissaldi,[13] R. D. Blandford,[2] E. D. Bloom,[2] R. Bonino,[14,15] E. Bottacini,[2] T. J. Brandt,[16] J. Bregeon,[17] P. Bruel,[18] R. Buehler,[1] G. A. Caliandro,[2,19] R. A. Cameron,[2] R. Caputo,[5] M. Caragiulo,[13] P. A. Caraveo,[20] C. Cecchi,[21,22] E. Charles,[2] A. Chekhtman,[23] J. Chiang,[2] G. Chiaro,[10] S. Ciprini,[24,21,25] R. Claus,[2] J. Cohen-Tanugi,[17] J. Conrad,[3,4,26] A. Cuoco,[14,15] S. Cutini,[24,25,21] F. D'Ammando,[27,28] A. de Angelis,[29] F. de Palma,[13,30] R. Desiante,[31,14] S. W. Digel,[2] L. Di Venere,[32] P. S. Drell,[2] A. Drlica-Wagner,[33,†] R. Essig,[34] C. Favuzzi,[32,13] S. J. Fegan,[18] E. C. Ferrara,[16] W. B. Focke,[2] A. Franckowiak,[2] Y. Fukazawa,[35] S. Funk,[36] P. Fusco,[32,13] F. Gargano,[13] D. Gasparrini,[24,25,21] N. Giglietto,[32,13] F. Giordano,[32,13] M. Giroletti,[27] T. Glanzman,[2] G. Godfrey,[2] G. A. Gomez-Vargas,[37,38] I. A. Grenier,[39] S. Guiriec,[16,40] M. Gustafsson,[41] E. Hays,[16] J.W. Hewitt,[42] D. Horan,[18] T. Jogler,[2] G. Jóhannesson,[43] M. Kuss,[12] S. Larsson,[44,4] L. Latronico,[14] J. Li,[45] L. Li,[44,4] M. Llena Garde,[3,4] F. Longo,[7,8] F. Loparco,[32,13] P. Lubrano,[21,22] D. Malyshev,[2] M. Mayer,[1] M. N. Mazziotta,[13] J. E. McEnery,[16,46] M. Meyer,[3,4] P. F. Michelson,[2] T. Mizuno,[47] A. A. Moiseev,[48,46] M. E. Monzani,[2] A. Morselli,[37] S. Murgia,[49] E. Nuss,[17] T. Ohsugi,[47] M. Orienti,[27] E. Orlando,[2] J. F. Ormes,[50] D. Paneque,[51,2] J. S. Perkins,[16] M. Pesce-Rollins,[12,2] F. Piron,[17] G. Pivato,[12] T. A. Porter,[2] S. Rainò,[32,13] R. Rando,[9,10] M. Razzano,[12,52] A. Reimer,[53,2] O. Reimer,[53,2] S. Ritz,[5] M. Sánchez-Conde,[4,3] A. Schulz,[1] N. Sehgal,[54] C. Sgrò,[12] E. J. Siskind,[55] F. Spada,[12] G. Spandre,[12] P. Spinelli,[32,13] L. Strigari,[56] H. Tajima,[57,2] H. Takahashi,[35] J. B. Thayer,[2] L. Tibaldo,[2] D. F. Torres,[45,58] E. Troja,[16,46] G. Vianello,[2] M. Werner,[53] B. L. Winer,[59] K. S. Wood,[60] M. Wood,[2,‡] G. Zaharijas,[61,62] and S. Zimmer[3,4]

(The Fermi-LAT Collaboration)

[1] *Deutsches Elektronen Synchrotron DESY, D-15738 Zeuthen, Germany*
[2] *W. W. Hansen Experimental Physics Laboratory, Kavli Institute for Particle Astrophysics and Cosmology, Department of Physics and SLAC National Accelerator Laboratory, Stanford University, Stanford, CA 94305, USA*
[3] *Department of Physics, Stockholm University, AlbaNova, SE-106 91 Stockholm, Sweden*
[4] *The Oskar Klein Centre for Cosmoparticle Physics, AlbaNova, SE-106 91 Stockholm, Sweden*
[5] *Santa Cruz Institute for Particle Physics, Department of Physics and Department of Astronomy and Astrophysics, University of California at Santa Cruz, Santa Cruz, CA 95064, USA*
[6] *Università di Pisa and Istituto Nazionale di Fisica Nucleare, Sezione di Pisa I-56127 Pisa, Italy*
[7] *Istituto Nazionale di Fisica Nucleare, Sezione di Trieste, I-34127 Trieste, Italy*
[8] *Dipartimento di Fisica, Università di Trieste, I-34127 Trieste, Italy*
[9] *Istituto Nazionale di Fisica Nucleare, Sezione di Padova, I-35131 Padova, Italy*
[10] *Dipartimento di Fisica e Astronomia "G. Galilei", Università di Padova, I-35131 Padova, Italy*
[11] *Dept. of Physics and Wisconsin IceCube Particle Astrophysics Center, University of Wisconsin, Madison, WI 53706, USA*
[12] *Istituto Nazionale di Fisica Nucleare, Sezione di Pisa, I-56127 Pisa, Italy*
[13] *Istituto Nazionale di Fisica Nucleare, Sezione di Bari, I-70126 Bari, Italy*
[14] *Istituto Nazionale di Fisica Nucleare, Sezione di Torino, I-10125 Torino, Italy*
[15] *Dipartimento di Fisica Generale "Amadeo Avogadro" , Università degli Studi di Torino, I-10125 Torino, Italy*
[16] *NASA Goddard Space Flight Center, Greenbelt, MD 20771, USA*
[17] *Laboratoire Univers et Particules de Montpellier, Université Montpellier, CNRS/IN2P3, Montpellier, France*
[18] *Laboratoire Leprince-Ringuet, École polytechnique, CNRS/IN2P3, Palaiseau, France*
[19] *Consorzio Interuniversitario per la Fisica Spaziale (CIFS), I-10133 Torino, Italy*
[20] *INAF-Istituto di Astrofisica Spaziale e Fisica Cosmica, I-20133 Milano, Italy*
[21] *Istituto Nazionale di Fisica Nucleare, Sezione di Perugia, I-06123 Perugia, Italy*
[22] *Dipartimento di Fisica, Università degli Studi di Perugia, I-06123 Perugia, Italy*
[23] *College of Science, George Mason University, Fairfax, VA 22030, resident at Naval Research Laboratory, Washington, DC 20375, USA*
[24] *Agenzia Spaziale Italiana (ASI) Science Data Center, I-00133 Roma, Italy*
[25] *INAF Osservatorio Astronomico di Roma, I-00040 Monte Porzio Catone (Roma), Italy*
[26] *Wallenberg Academy Fellow*
[27] *INAF Istituto di Radioastronomia, I-40129 Bologna, Italy*
[28] *Dipartimento di Astronomia, Università di Bologna, I-40127 Bologna, Italy*

Operated by Fermi Research Alliance, LLC under Contract No. De-AC02-07CH11359 with the United States Department of Energy.

[29] *Dipartimento di Fisica, Università di Udine and Istituto Nazionale di Fisica Nucleare, Sezione di Trieste, Gruppo Collegato di Udine, I-33100 Udine*
[30] *Università Telematica Pegaso, Piazza Trieste e Trento, 48, I-80132 Napoli, Italy*
[31] *Università di Udine, I-33100 Udine, Italy*
[32] *Dipartimento di Fisica "M. Merlin" dell'Università e del Politecnico di Bari, I-70126 Bari, Italy*
[33] *Center for Particle Astrophysics, Fermi National Accelerator Laboratory, Batavia, IL 60510, USA*
[34] *C.N. Yang Institute for Theoretical Physics, State University of New York, Stony Brook, NY 11794-3840, U.S.A., USA*
[35] *Department of Physical Sciences, Hiroshima University, Higashi-Hiroshima, Hiroshima 739-8526, Japan*
[36] *Erlangen Centre for Astroparticle Physics, D-91058 Erlangen, Germany*
[37] *Istituto Nazionale di Fisica Nucleare, Sezione di Roma "Tor Vergata", I-00133 Roma, Italy*
[38] *Departamento de Fisíca, Pontificia Universidad Católica de Chile, Avenida Vicuña Mackenna 4860, Santiago, Chile*
[39] *Laboratoire AIM, CEA-IRFU/CNRS/Université Paris Diderot, Service d'Astrophysique, CEA Saclay, F-91191 Gif sur Yvette, France*
[40] *NASA Postdoctoral Program Fellow, USA*
[41] *Georg-August University Göttingen, Institute for theoretical Physics - Faculty of Physics, Friedrich-Hund-Platz 1, D-37077 Göttingen, Germany*
[42] *University of North Florida, Department of Physics, 1 UNF Drive, Jacksonville, FL 32224 , USA*
[43] *Science Institute, University of Iceland, IS-107 Reykjavik, Iceland*
[44] *Department of Physics, KTH Royal Institute of Technology, AlbaNova, SE-106 91 Stockholm, Sweden*
[45] *Institute of Space Sciences (IEEC-CSIC), Campus UAB, E-08193 Barcelona, Spain*
[46] *Department of Physics and Department of Astronomy, University of Maryland, College Park, MD 20742, USA*
[47] *Hiroshima Astrophysical Science Center, Hiroshima University, Higashi-Hiroshima, Hiroshima 739-8526, Japan*
[48] *Center for Research and Exploration in Space Science and Technology (CRESST) and NASA Goddard Space Flight Center, Greenbelt, MD 20771, USA*
[49] *Center for Cosmology, Physics and Astronomy Department, University of California, Irvine, CA 92697-2575, USA*
[50] *Department of Physics and Astronomy, University of Denver, Denver, CO 80208, USA*
[51] *Max-Planck-Institut für Physik, D-80805 München, Germany*
[52] *Funded by contract FIRB-2012-RBFR12PM1F from the Italian Ministry of Education, University and Research (MIUR)*
[53] *Institut für Astro- und Teilchenphysik and Institut für Theoretische Physik, Leopold-Franzens-Universität Innsbruck, A-6020 Innsbruck, Austria*
[54] *Physics and Astronomy Department, Stony Brook University, Stony Brook, NY 11794, USA*
[55] *NYCB Real-Time Computing Inc., Lattingtown, NY 11560-1025, USA*
[56] *Texas A&M University, Department of Physics and Astronomy, College Station, TX 77843-4242, USA*
[57] *Solar-Terrestrial Environment Laboratory, Nagoya University, Nagoya 464-8601, Japan*
[58] *Institució Catalana de Recerca i Estudis Avançats (ICREA), Barcelona, Spain*
[59] *Department of Physics, Center for Cosmology and Astro-Particle Physics, The Ohio State University, Columbus, OH 43210, USA*
[60] *Space Science Division, Naval Research Laboratory, Washington, DC 20375-5352, USA*
[61] *Istituto Nazionale di Fisica Nucleare, Sezione di Trieste, and Università di Trieste, I-34127 Trieste, Italy*
[62] *Laboratory for Astroparticle Physics, University of Nova Gorica, Vipavska 13, SI-5000 Nova Gorica, Slovenia*
(Dated: November 4, 2015)

The dwarf spheroidal satellite galaxies (dSphs) of the Milky Way are some of the most dark matter (DM) dominated objects known. We report on gamma-ray observations of Milky Way dSphs based on 6 years of *Fermi* Large Area Telescope data processed with the new `Pass 8` event-level analysis. None of the dSphs are significantly detected in gamma rays, and we present upper limits on the DM annihilation cross section from a combined analysis of 15 dSphs. These constraints are among the strongest and most robust to date and lie below the canonical thermal relic cross section for DM of mass $\lesssim 100\,\mathrm{GeV}$ annihilating via quark and τ-lepton channels.

PACS numbers: 95.35.+d, 95.85.Pw, 98.52.Wz
Keywords: dark matter; gamma rays; dwarf galaxies

INTRODUCTION

Approximately 26% of the energy density of the universe is composed of non-baryonic cold dark matter (DM) [1]. Weakly interacting massive particles (WIMPs) are an attractive candidate to constitute some or all of DM [2–4]. The relic abundance of WIMPs is determined by their annihilation cross section at freeze-out [5], and the characteristic weak-scale cross sections of WIMPs can naturally produce a relic abundance equal

to the observed abundance of DM. Self-annihilation of WIMPs would continue today in regions of high DM density and result in the production of energetic Standard Model particles. The large mass of the WIMP ($m_{\rm DM}$) permits the production of gamma rays observable by the *Fermi* Large Area Telescope (LAT), which is sensitive to energies ranging from 20 MeV to $>300\,$GeV.

Kinematic data indicate that the dwarf spheroidal satellite galaxies (dSphs) of the Milky Way contain a substantial DM component [6, 7]. The gamma-ray signal flux at the LAT, ϕ_s ($\mathrm{ph\,cm^{-2}\,s^{-1}}$), expected from the annihilation of DM with a density distribution $\rho_{\rm DM}(\boldsymbol{r})$ is given by

$$\phi_s(\Delta\Omega) = \underbrace{\frac{1}{4\pi}\frac{\langle\sigma v\rangle}{2m_{\rm DM}^2}\int_{E_{\rm min}}^{E_{\rm max}}\frac{{\rm d}N_\gamma}{{\rm d}E_\gamma}{\rm d}E_\gamma}_{\text{particle physics}} \times \underbrace{\int_{\Delta\Omega}\int_{\rm l.o.s.}\rho^2_{\rm DM}(\boldsymbol{r}){\rm d}l{\rm d}\Omega'}_{\rm J-factor}\,. \quad (1)$$

Here, the first term is dependent on the particle physics properties — i.e., the thermally-averaged annihilation cross section, $\langle\sigma v\rangle$, the particle mass, $m_{\rm DM}$, and the differential gamma-ray yield per annihilation, ${\rm d}N_\gamma/{\rm d}E_\gamma$, integrated over the experimental energy range.[1] The second term, known as the J-factor, is the line-of-sight (l.o.s.) integral through the DM distribution integrated over a solid angle, $\Delta\Omega$.

Milky Way dSphs can give rise to J-factors in excess of $10^{19}\,\mathrm{GeV^2\,cm^{-5}}$ [8, 9], which, coupled with their lack of non-thermal astrophysical processes, makes them good targets for DM searches via gamma rays. Gamma-ray searches for dSphs yield some of the most stringent constraints on $\langle\sigma v\rangle$, particularly when multiple dSphs are analyzed together using a joint likelihood technique [10–15]. Limits on $\langle\sigma v\rangle$ derived from observations of dSphs have begun to probe the low-$m_{\rm DM}$ parameter space for which the WIMP abundance matches the observed DM relic density.

In contrast, DM searches in the Galactic center take advantage of a J-factor that is $\mathcal{O}(100)$ times larger, although gamma-ray emission from non-thermal processes makes a bright, structured background. Several studies of the Galactic center interpret an excess of gamma rays with respect to modeled astrophysical backgrounds as a signal of 20 to 50 GeV WIMPs annihilating via the $b\bar{b}$ channel [16–19]. Coincidentally, the largest deviation from expected background in some previous studies of dSphs occurred for a similar set of WIMP characteristics; however, this deviation was not statistically significant [13].

Using a new LAT event-level analysis, known as `Pass 8`, we re-examine the sample of 25 Milky Way dSphs from Ackermann *et al.* [13] using six years of LAT data. The `Pass 8` data benefits from an improved point-spread function (PSF), effective area, and energy reach. More accurate Monte Carlo simulations of the detector and the environment in low-Earth orbit have reduced the systematic uncertainty in the LAT instrument response functions (IRFs) [20]. Within the standard photon classes, `Pass 8` offers *event types*, subdivisions based on event-by-event uncertainties in the directional and energy measurements, which can increase the sensitivity of likelihood-based analyses. In this work we use a set of four PSF event-type selections that subdivide the events in our data sample according to the quality of their directional reconstruction. In addition to the improvements from `Pass 8`, we employ the updated third LAT source catalog (3FGL), based on four years of `Pass 7 Reprocessed` data, to model point-like background sources [21]. Together, these improvements, along with an additional two years of data taking, lead to a predicted increase in sensitivity of 70% relative to the four-year analysis of Ackermann *et al.* [13] for the $b\bar{b}$ channel at 100 GeV. More details on `Pass 8` and other aspects of this analysis can be found in Supplemental Material [22].

LAT DATA SELECTION

We examine six years of LAT data (2008-08-04 to 2014-08-05) selecting `Pass 8` SOURCE-class events in the energy range between 500 MeV and 500 GeV. We selected the 500 MeV lower limit to mitigate the impact of leakage from the bright limb of the Earth because the PSF broadens considerably below that energy. To further avoid contamination from terrestrial gamma rays, events with zenith angles larger than 100° are rejected. We also remove time intervals around bright GRBs and solar flares following the prescription used for the 3FGL catalog. We extract from this data set $10^\circ\times10^\circ$ square regions of interest (ROIs) in Galactic coordinates centered at the position of each dSph specified in Table I.

At a given energy, 20%–40% of the events classified as photons in our six-year `Pass 8` data set are shared with the analysis of Ackermann *et al.* [13]. The low fraction of shared events can be attributed primarily to the larger time range used for the present analysis (four versus six years) and the increase in gamma-ray acceptance of the P8R2_SOURCE event class relative to P7REP_CLEAN. At most, the `Pass 7` events can represent 35%–50% of the new, larger sample. Migration of the individual recon-

[1] Strictly speaking, the differential yield per annihilation in Equation (1) is a sum of differential yields into specific final states: ${\rm d}N_\gamma/{\rm d}E_\gamma = \sum_f B_f\,{\rm d}N^f_\gamma/{\rm d}E_\gamma$, where B_f is the branching fraction into final state f. Here, we make use of Equation (1) in the context of single final states only.

structed events, particularly residual cosmic rays, across ROI and class selection boundaries further reduces the overlap, making the two analyses nearly statistically independent [22].

J-FACTORS FOR DWARF SPHEROIDAL GALAXIES

The DM content of dSphs can be determined through dynamical modeling of their stellar density and velocity dispersion profiles [23–25]. Recent studies have shown that an accurate estimate of the dynamical mass of a dSph can be derived from measurements of the average stellar velocity dispersion and half-light radius alone [26, 27]. The total mass within the half-light radius and the integrated J-factor have been found to be fairly insensitive to the assumed DM density profile [13, 25, 28]. We assume that the DM distribution in dSphs follows a Navarro-Frenk-White (NFW) profile [29],

$$\rho_{\rm DM}(r) = \frac{\rho_0 r_s^3}{r(r_s + r)^2}, \qquad (2)$$

where r_s and ρ_0 are the NFW scale radius and characteristic density, respectively. We take J-factors and other physical properties for the Milky Way dSphs from Ackermann *et al.* [13] (and references therein).

DATA ANALYSIS

We perform a binned Poisson maximum-likelihood analysis in 24 bins of energy,[2] logarithmically spaced from 500 MeV to 500 GeV, and an 0.1° angular pixelization. The low-energy bound of 500 MeV is selected to mitigate the impact of leakage from the bright limb of the Earth because the PSF broadens considerably below that energy. The high-energy bound of 500 GeV is chosen to mitigate the effect of the increasing residual charged-particle background at higher energies [30]. The data were analyzed with the Fermi Science Tools[3] version 10-01-01 and the P8R2_SOURCE_V6 IRFs. Our diffuse background model includes a structured Galactic component and a spatially isotropic component that represents both extragalactic emission and residual particle contamination.[4] Because the energy resolution of the LAT was not accounted for when fitting the Galactic diffuse model, differences in response (energy resolution and effective area) between IRF sets lead to different measured intensities for this component. Thus, a small energy-dependent scaling has been applied to the `Pass 7 Reprocessed` Galactic diffuse model. Changes with respect to the `Pass 7 Reprocessed` model are less than 5% above 100 MeV. Details on the derivation of the rescaled model are given in [22]. The gamma-ray characteristics of nearby point-like sources are taken from the 3FGL catalog [21].

We perform a bin-by-bin likelihood analysis of the gamma-ray emission coincident with each dSph following the procedure of Ackermann *et al.* [13]. The flux normalizations of the Galactic diffuse and isotropic components and 3FGL catalog sources within the $10° \times 10°$ ROI were fit simultaneously in a binned likelihood analysis over the broadband energy range from 500 MeV to 500 GeV. The normalizations of the background sources are insensitive to the inclusion of a putative power-law source at the locations of the dSphs, which is consistent with the lack of any strong signal associated with the dSphs. Fixing the normalizations of the background sources with the broad-band fit before fitting each bin individually avoids numerical instability resulting from the fine binning in energy and the degeneracy of the diffuse background components at high Galactic latitudes.

After fixing the background normalizations, we scan the likelihood as a function of the flux normalization of the putative DM signal independently in each energy bin (this procedure is similar to that used to evaluate the spectral energy distribution of a source). Within each bin, we model the putative dSph source with a power-law spectral model ($\mathrm{d}N/\mathrm{d}E \propto E^{-\Gamma}$) with spectral index of $\Gamma = 2$. By analyzing each energy bin separately, we avoid selecting a single spectral shape to span the entire energy range at the expense of introducing additional degrees of freedom into the fit.

While the bin-by-bin likelihood function is essentially independent of spectral assumptions, it does depend on the spatial model of the DM distribution in the dSphs. We model the dSphs with spatially extended NFW DM density profiles projected along the line of sight. The angular extent of the emission profile for each dSph is set by the scale radius of its DM halo, which contains approximately 90% of the total annihilation flux. We use the set of DM halo scale radii from Ackermann *et al.* [13], which span a range of subtended angles between 0.1° and 0.4°.

We test a wide range of DM annihilation hypotheses by using predicted gamma-ray spectra to tie the signal normalization across the energy bins. Spectra for DM annihilation are generated with the `DMFIT` package based on `Pythia` 8.165 [13, 31, 32]. We reconstruct a broad-band likelihood function by multiplying the bin-by-bin likelihood functions evaluated at the predicted fluxes for a given DM model.

We combine the broad-band likelihood functions across

[2] Constraints are insensitive to finer binning.
[3] http://fermi.gsfc.nasa.gov/ssc/data/analysis/software
[4] http://fermi.gsfc.nasa.gov/ssc/data/access/lat/BackgroundModels.html

15 of the observed dSphs[5] and include statistical uncertainties on the J-factors of each dSph by adding an additional J-factor likelihood term to the binned Poisson likelihood for the LAT data. The J-factor likelihood for target i is given by

$$\mathcal{L}_J(J_i \,|\, J_{\rm obs,i}, \sigma_i) = \frac{1}{\ln(10) J_{\rm obs,i}\sqrt{2\pi}\sigma_i} \times e^{-(\log_{10}(J_i)-\log_{10}(J_{\rm obs,i}))^2/2\sigma_i^2}, \quad (3)$$

where J_i is the true value of the J-factor and $J_{\rm obs,i}$ is the measured J-factor with error σ_i. This parameterization of the J-factor likelihood is obtained by fitting a log-normal function with peak value $J_{\rm obs,i}$ to the posterior distribution for each J-factor as derived by Martinez [8], providing a reasonable way to quantify the uncertainties on the J-factors. This approach is a slight modification of the approach in Ackermann *et al.* [10, 13], where an effective likelihood was derived considering a flat prior on the J-factors. We note that the J-factor correction is only intended to incorporate the *statistical* uncertainty in the J-factors, and not the systematic uncertainty resulting from the fitting procedure or choice of priors [22]. More details on the derivation of the J-factor likelihood and the effects of systematic uncertainties can be found in Supplemental Material [22].

Combining the broad-band gamma-ray and J-factor likelihood functions, our likelihood function for target i becomes,

$$\tilde{\mathcal{L}}_i(\boldsymbol{\mu}, \boldsymbol{\theta}_i = \{\boldsymbol{\alpha}_i, J_i\} \,|\, \mathcal{D}_i) = \mathcal{L}_i(\boldsymbol{\mu}, \boldsymbol{\theta}_i \,|\, \mathcal{D}_i)\mathcal{L}_J(J_i \,|\, J_{\rm obs,i}, \sigma_i). \quad (4)$$

Here, $\boldsymbol{\mu}$ are the parameters of the DM model, $\boldsymbol{\theta}_i$ is the set of nuisance parameters that includes both nuisance parameters from the LAT analysis ($\boldsymbol{\alpha}_i$) and the dSph J-factor (J_i), and $\mathcal{D}_i$ is the gamma-ray data. We incorporate additional information about the event-wise quality of the angular reconstruction by forming the LAT likelihood function ($\mathcal{L}_i$) from the product of likelihood functions for four PSF event types. The four PSF event types (PSF0, PSF1, PSF2, and PSF3) subdivide the events in the SOURCE-class data set into exclusive partitions ($\mathcal{D}_{i,j}$) in order of decreasing uncertainty on the direction measurement. The resulting joint LAT likelihood function is given by

$$\mathcal{L}_i(\boldsymbol{\mu}, \boldsymbol{\theta}_i \,|\, \mathcal{D}_i) = \prod_j \mathcal{L}_i(\boldsymbol{\mu}, \boldsymbol{\theta}_i \,|\, \mathcal{D}_{i,j}). \quad (5)$$

The spectral and spatial model of gamma-ray counts for each event type partition is evaluated using a set of IRFs computed for that class and type selection.

We evaluate the significance of DM hypotheses using a test statistic (TS) defined as

$$\mathrm{TS} = -2\ln\left(\frac{\mathcal{L}(\boldsymbol{\mu}_0, \hat{\boldsymbol{\theta}} \,|\, \mathcal{D})}{\mathcal{L}(\hat{\boldsymbol{\mu}}, \hat{\boldsymbol{\theta}} \,|\, \mathcal{D})}\right), \quad (6)$$

where $\boldsymbol{\mu}_0$ are the parameters of the null (no DM) hypothesis and $\hat{\boldsymbol{\mu}}$ and $\hat{\boldsymbol{\theta}}$ are the best-fit parameters under the DM hypothesis. $\mathcal{L}$ can here be either the likelihood for an individual dSph or the joint likelihood for the dSphs in our combined sample. We note that following the methodology of Ackermann *et al.* [13] we use background parameters ($\hat{\boldsymbol{\theta}}$) derived under the hypothesis of a DM source with a $\Gamma = 2$ power-law spectrum when evaluating both the null and DM hypotheses. This is a good approximation as long as the best-fit signal is small relative to the background in the ROI. Based on the asymptotic theorem of Chernoff [33], the TS can be converted to a significance based on a mixture of χ^2 distributions. The validity of this assumption is examined further in Supplemental Material [22].

RESULTS

We find no significant gamma-ray excess associated with the Milky Way dSphs when analyzed individually or as a population. In the combined analysis of 15 dSphs, the largest deviation from the background-only hypothesis has TS = 1.3 occurring for $m_{\rm DM} = 2\,$GeV annihilating through the e^+e^- channel. Among the dSphs in our combined analysis, the dSph with the largest individual significance is Sculptor with TS = 4.3 for $m_{\rm DM} = 5\,$GeV annihilating through the $\mu^+\mu^-$ channel. The maximum TS of our combined analysis is well below the threshold set for gamma-ray source detection and is completely consistent with a background fluctuation [21]. We set upper limits on $\langle\sigma v\rangle$ at 95% confidence level (CL) for WIMPs with $m_{\rm DM}$ between 2 GeV and 10 TeV annihilating into six different standard model channels ($b\bar{b}$, $\tau^+\tau^-$, $\mu^+\mu^-$, e^+e^-, W^+W^-, $u\bar{u}$). [6] Figure 1 shows the comparison of the limits for the $b\bar{b}$ and $\tau^+\tau^-$ channels with expectation bands derived from the analysis of 300 randomly selected sets of blank fields. Sets of blank fields are generated by choosing random sky positions with $|b| > 30^\circ$ that are centered at least 0.5° from 3FGL catalog sources. We additionally require fields within each set to be separated by at least 7°. Our expected limit bands are evaluated with the 3FGL source catalog based on four years of `Pass 7 Reprocessed` data and account for the influence of new sources present in the six-year `Pass 8` data set.

[5] Selected to have kinematically determined J-factors and avoid ROI overlap. The set is identical to that in Ackermann *et al.* [13].

[6] Results for all channels as well as bin-by-bin likelihood functions for each target are available in machine-readable format at: http://www-glast.stanford.edu/pub_data/1048/.

Comparing with the results of Ackermann *et al.* [13], we find a factor of 3–5 improvement in the limits for all channels using six years of `Pass 8` data and the same sample of 15 dSphs. The larger data set as well as the gains in the LAT instrument performance enabled by `Pass 8` both contribute to the increased sensitivity of the present analysis. An additional 30–40% improvement in the limit can be attributed to the modified functional form chosen for the J-factor likelihood (Equation 3). Statistical fluctuations in the `Pass 8` data set also play a substantial role. Because the `Pass 8` six-year and `Pass 7 Reprocessed` four-year event samples have a shared fraction of only 20–40%, the two analyses are nearly statistically independent. For masses below 100 GeV, the upper limits of Ackermann *et al.* [13] were near the 95% upper bound of the expected sensitivity band while the limits in the present analysis are within one standard deviation of the median expectation value.

Uncertainties in the LAT IRFs, modeling of the diffuse background, and estimation of J-factors all contribute systematic errors to this analysis. By examining maximal variations of each contributor, we find that at 100 GeV they lead to ±9%, ±8%, and ±33% shifts in our limits, respectively (see Supplemental Material [22]).

Our results begin to constrain some of the preferred parameter space for a DM interpretation of a gamma-ray excess in the Galactic center region [16–19]. As shown in Figure 2, for interpretations assuming a $b\bar{b}$ final state, the best-fit models lie in a region of parameter space slightly above the 95% CL upper limit from this analysis, with an annihilation cross section in the range of $(1\text{–}3)\times10^{-26}\,\mathrm{cm^3\,s^{-1}}$ and m_{DM} between 25 and 50 GeV. However, uncertainties in the structure of the Galactic DM distribution can significantly enlarge the best-fit regions of $\langle\sigma v\rangle$, channel, and m_{DM} [38].

In conclusion, we present a combined analysis of 15 Milky Way dSphs using a new and improved LAT data set processed with the `Pass 8` event-level analysis. We exclude the thermal relic annihilation cross section ($\sim 2.2\times 10^{-26}\,\mathrm{cm^3\,s^{-1}}$) for WIMPs with $m_{\mathrm{DM}} \lesssim 100$ GeV annihilating through the quark and τ-lepton channels. Our results also constrain DM particles with m_{DM} above 100 GeV surpassing the best limits from Imaging Atmospheric Cherenkov Telescopes for masses up to $\sim$1 TeV for quark channels and $\sim$300 GeV for the τ-lepton channel. These constraints include the statistical uncertainty on the DM content of the dSphs. The future sensitivity to DM annihilation in dSphs will benefit from additional LAT data taking and the discovery of new dSphs with upcoming optical surveys such as the Dark Energy Survey [39] and the Large Synoptic Survey Telescope [40].

TABLE I. Properties of Milky Way dSphs.

Name	ℓ[a] (deg)	b[a] (deg)	Distance (kpc)	$\log_{10}(J_{\mathrm{obs}})$[b] ($\log_{10}[\mathrm{GeV^2\,cm^{-5}}]$)	Ref.
Bootes I	358.1	69.6	66	18.8 ± 0.22	[41]
Canes Venatici II	113.6	82.7	160	17.9 ± 0.25	[42]
Carina	260.1	−22.2	105	18.1 ± 0.23	[43]
Coma Berenices	241.9	83.6	44	19.0 ± 0.25	[42]
Draco	86.4	34.7	76	18.8 ± 0.16	[44]
Fornax	237.1	−65.7	147	18.2 ± 0.21	[43]
Hercules	28.7	36.9	132	18.1 ± 0.25	[42]
Leo II	220.2	67.2	233	17.6 ± 0.18	[45]
Leo IV	265.4	56.5	154	17.9 ± 0.28	[42]
Sculptor	287.5	−83.2	86	18.6 ± 0.18	[43]
Segue 1	220.5	50.4	23	19.5 ± 0.29	[46]
Sextans	243.5	42.3	86	18.4 ± 0.27	[43]
Ursa Major II	152.5	37.4	32	19.3 ± 0.28	[42]
Ursa Minor	105.0	44.8	76	18.8 ± 0.19	[44]
Willman 1	158.6	56.8	38	19.1 ± 0.31	[47]
Bootes II[c]	353.7	68.9	42	–	–
Bootes III	35.4	75.4	47	–	–
Canes Venatici I	74.3	79.8	218	17.7 ± 0.26	[42]
Canis Major	240.0	−8.0	7	–	–
Leo I	226.0	49.1	254	17.7 ± 0.18	[48]
Leo V	261.9	58.5	178	–	–
Pisces II	79.2	−47.1	182	–	–
Sagittarius	5.6	−14.2	26	–	–
Segue 2	149.4	−38.1	35	–	–
Ursa Major I	159.4	54.4	97	18.3 ± 0.24	[42]

[a] Galactic longitude and latitude.
[b] J-factors are calculated assuming an NFW density profile and integrated over a circular region with a solid angle of $\Delta\Omega \sim 2.4\times10^{-4}$ sr (angular radius of 0.5°).
[c] dSphs below the horizontal line are not included in the combined analysis.

ACKNOWLEDGMENTS

The *Fermi*-LAT Collaboration acknowledges support for LAT development, operation and data analysis from NASA and DOE (United States), CEA/Irfu and IN2P3/CNRS (France), ASI and INFN (Italy), MEXT, KEK, and JAXA (Japan), and the K.A. Wallenberg Foundation, the Swedish Research Council and the National Space Board (Sweden). Science analysis support in the operations phase from INAF (Italy) and CNES (France) is also gratefully acknowledged.

* brandon.anderson@fysik.su.se
† kadrlica@fnal.gov
‡ mdwood@slac.stanford.edu

[1] R. Adam *et al.* (Planck Collaboration), (2015), arXiv:1502.01582 [astro-ph.CO].
[2] G. Jungman, M. Kamionkowski, and K. Griest, Phys. Rep. **267**, 195 (1996), arXiv:hep-ph/9506380 [hep-ph].

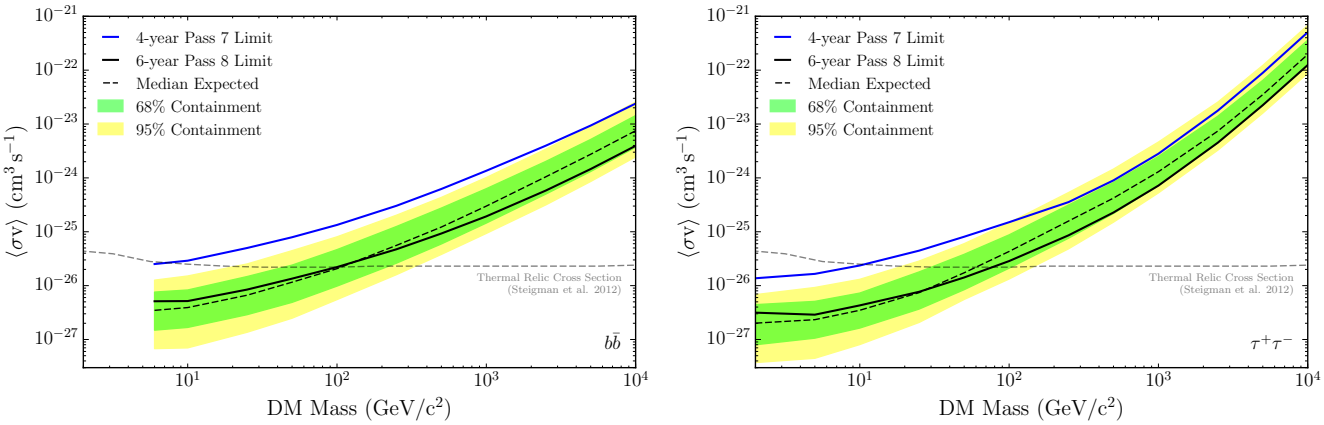

FIG. 1. Constraints on the DM annihilation cross section at 95% CL for the $b\bar{b}$ (left) and $\tau^+\tau^-$ (right) channels derived from a combined analysis of 15 dSphs. Bands for the expected sensitivity are calculated by repeating the same analysis on 300 randomly selected sets of high-Galactic-latitude blank fields in the LAT data. The dashed line shows the median expected sensitivity while the bands represent the 68% and 95% quantiles. For each set of random locations, nominal J-factors are randomized in accord with their measurement uncertainties. The solid blue curve shows the limits derived from a previous analysis of four years of `Pass 7 Reprocessed` data and the same sample of 15 dSphs [13]. The dashed gray curve in this and subsequent figures corresponds to the thermal relic cross section from Steigman *et al.* [5].

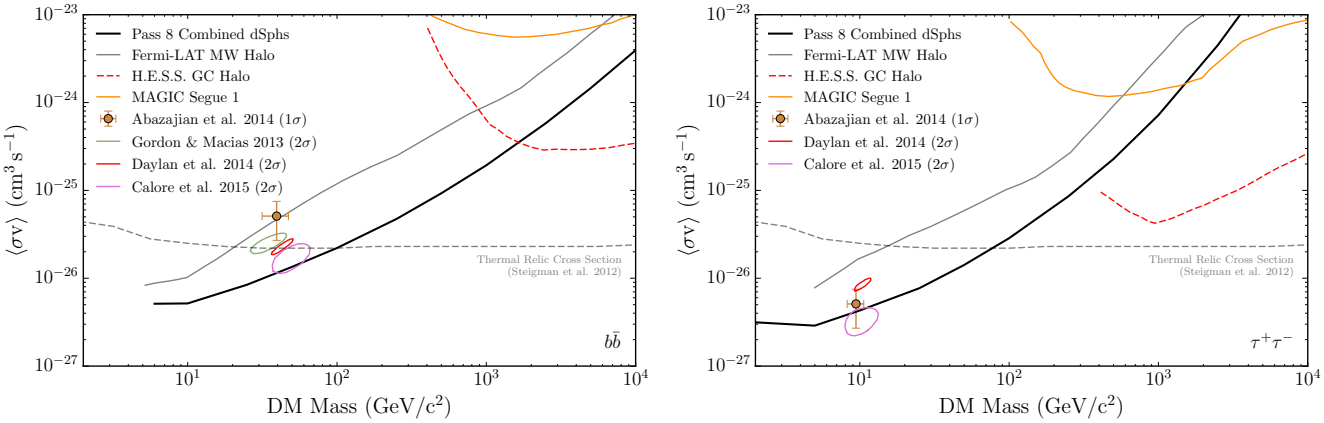

FIG. 2. Comparison of constraints on the DM annihilation cross section for the $b\bar{b}$ (left) and $\tau^+\tau^-$ (right) channels from this work with previously published constraints from LAT analysis of the Milky Way halo (3σ limit) [34], 112 hours of observations of the Galactic Center with H.E.S.S. [35], and 157.9 hours of observations of Segue 1 with MAGIC [36]. Pure annihilation channel limits for the Galactic Center H.E.S.S. observations are taken from Abazajian and Harding [37] and assume an Einasto Milky Way density profile with $\rho_\odot = 0.389\,\mathrm{GeV\,cm^{-3}}$. Closed contours and the marker with error bars show the best-fit cross section and mass from several interpretations of the Galactic center excess [16–19].

[3] L. Bergstrom, Rept. Prog. Phys. **63**, 793 (2000), arXiv:hep-ph/0002126 [hep-ph].
[4] G. Bertone, D. Hooper, and J. Silk, Phys. Rep. **405**, 279 (2005), arXiv:hep-ph/0404175 [hep-ph].
[5] G. Steigman, B. Dasgupta, and J. F. Beacom, Phys. Rev. D **86**, 023506 (2012), arXiv:1204.3622 [hep-ph].
[6] M. Mateo, Annu. Rev. Astron. Astrophys. **36**, 435 (1998), arXiv:astro-ph/9810070 [astro-ph].
[7] A. W. McConnachie, Astron.J. **144**, 4 (2012), arXiv:1204.1562 [astro-ph.CO].
[8] G. D. Martinez, Mon. Not. R. Astron. Soc. **451**, 2524 (2015), arXiv:1309.2641 [astro-ph.GA].
[9] A. Geringer-Sameth, S. M. Koushiappas, and M. Walker, (2014), arXiv:1408.0002 [astro-ph.CO].
[10] M. Ackermann *et al.* (Fermi-LAT Collaboration), Phys. Rev. Lett. **107**, 241302 (2011), arXiv:1108.3546 [astro-ph.HE].
[11] A. Geringer-Sameth and S. M. Koushiappas, Phys. Rev. Lett. **107**, 241303 (2011), arXiv:1108.2914 [astro-ph.CO].
[12] M. N. Mazziotta, F. Loparco, F. de Palma, and N. Giglietto, Astropart. **37**, 26 (2012), arXiv:1203.6731 [astro-ph.IM].
[13] M. Ackermann *et al.* (Fermi-LAT Collaboration), Phys. Rev. D **89**, 042001 (2014), arXiv:1310.0828 [astro-ph.HE].
[14] A. Geringer-Sameth, S. M. Koushiappas, and M. G. Walker, (2014), arXiv:1410.2242 [astro-ph.CO].

[15] B. Anderson, J. Chiang, J. Cohen-Tanugi, J. Conrad, A. Drlica-Wagner, M. Llena Garde, and Stephan Zimmer for the Fermi-LAT Collaboration, ArXiv e-prints (2015), arXiv:1502.03081 [astro-ph.HE].

[16] T. Daylan, D. P. Finkbeiner, D. Hooper, T. Linden, S. K. N. Portillo, *et al.*, (2014), arXiv:1402.6703 [astro-ph.HE].

[17] C. Gordon and O. Macias, Phys. Rev. D **88**, 083521 (2013), arXiv:1306.5725 [astro-ph.HE].

[18] K. N. Abazajian, N. Canac, S. Horiuchi, and M. Kaplinghat, Phys. Rev. D **90**, 023526 (2014), arXiv:1402.4090 [astro-ph.HE].

[19] F. Calore, I. Cholis, and C. Weniger, JCAP **1503**, 038 (2015), arXiv:1409.0042 [astro-ph.CO].

[20] W. Atwood *et al.* (Fermi-LAT Collaboration), *2012 Fermi Symposium Proceedings*, eConf **C121028** (2013), arXiv:1303.3514 [astro-ph.IM].

[21] M. Ackermann *et al.* (The Fermi-LAT Collaboration), (2015), arXiv:1501.02003 [astro-ph.HE].

[22] See Supplemental Material for more details.

[23] M. G. Walker, "Dark Matter in the Milky Way's Dwarf Spheroidal Satellites," in *Planets, Stars and Stellar Systems. Volume 5: Galactic Structure and Stellar Populations* (2013) arXiv:1205.0311 [astro-ph.CO].

[24] G. Battaglia, A. Helmi, and M. Breddels, New Astron. Rev. **57**, 52 (2013), arXiv:1305.5965 [astro-ph.CO].

[25] L. E. Strigari, Phys. Rep. , 1 (2013), arXiv:1211.7090 [astro-ph.CO].

[26] M. G. Walker, M. Mateo, E. W. Olszewski, J. Penarrubia, N. Evans, *et al.*, Astrophys. J. **704**, 1274 (2009), arXiv:0906.0341 [astro-ph.CO].

[27] J. Wolf, G. D. Martinez, J. S. Bullock, M. Kaplinghat, M. Geha, *et al.*, Mon. Not. R. Astron. Soc. **406**, 1220 (2010), arXiv:0908.2995 [astro-ph.CO].

[28] G. D. Martinez, J. S. Bullock, M. Kaplinghat, L. E. Strigari, and R. Trotta, J. Cosmol. Astropart. Phys. **0906**, 014 (2009), arXiv:0902.4715 [astro-ph.HE].

[29] J. F. Navarro, C. S. Frenk, and S. D. White, Astrophys. J. **490**, 493 (1997), arXiv:astro-ph/9611107 [astro-ph].

[30] M. Ackermann *et al.* (The Fermi LAT Collaboration), Astrophys. J. **799**, 86 (2014), arXiv:1410.3696 [astro-ph.HE].

[31] T. E. Jeltema and S. Profumo, J. Cosmol. Astropart. Phys. **0811**, 003 (2008), arXiv:0808.2641 [astro-ph].

[32] T. Sjöstrand, S. Mrenna, and P. Z. Skands, Comput.Phys.Commun. **178**, 852 (2008), arXiv:0710.3820 [hep-ph].

[33] H. Chernoff, Ann. Math. Statist. **25**, 573 (1954).

[34] M. Ackermann *et al.* (Fermi-LAT Collaboration), Astrophys. J. **761**, 91 (2012), arXiv:1205.6474 [astro-ph.CO].

[35] A. Abramowski *et al.* (H.E.S.S. Collaboration), Phys. Rev. Lett. **106**, 161301 (2011), arXiv:1103.3266 [astro-ph.HE].

[36] J. Aleksić, S. Ansoldi, L. Antonelli, P. Antoranz, A. Babic, *et al.* (MAGIC Collaboration), J. Cosmol. Astropart. Phys. **1402**, 008 (2014), arXiv:1312.1535 [hep-ph].

[37] K. N. Abazajian and J. P. Harding, JCAP **1201**, 041 (2012), arXiv:1110.6151 [hep-ph].

[38] P. Agrawal, B. Batell, P. J. Fox, and R. Harnik, ArXiv e-prints (2014), arXiv:1411.2592 [hep-ph].

[39] T. Abbott *et al.* (DES Collaboration), (2005), arXiv:astro-ph/0510346 [astro-ph].

[40] Z. Ivezic, J. Tyson, R. Allsman, J. Andrew, and R. Angel (LSST Collaboration), (2008), arXiv:0805.2366 [astro-ph].

[41] M. Dall'Ora, G. Clementini, K. Kinemuchi, V. Ripepi, M. Marconi, *et al.*, Astrophys. J. **653**, L109 (2006), arXiv:astro-ph/0611285 [astro-ph].

[42] J. D. Simon and M. Geha, Astrophys. J. **670**, 313 (2007), arXiv:0706.0516 [astro-ph].

[43] M. G. Walker, M. Mateo, and E. W. Olszewski, Astron. J. **137**, 3100 (2009), arXiv:0811.0118.

[44] R. R. Muñoz, P. M. Frinchaboy, S. R. Majewski, J. R. Kuhn, M.-Y. Chou, *et al.*, Astrophys. J. **631**, L137 (2005), arXiv:astro-ph/0504035 [astro-ph].

[45] A. Koch, J. Kleyna, M. Wilkinson, E. Grebel, G. Gilmore, *et al.*, Astron. J. **134**, 566 (2007), arXiv:0704.3437 [astro-ph].

[46] J. D. Simon, M. Geha, Q. E. Minor, G. D. Martinez, E. N. Kirby, *et al.*, Astrophys. J. **733**, 46 (2011), arXiv:1007.4198 [astro-ph.GA].

[47] B. Willman, M. Geha, J. Strader, L. E. Strigari, J. D. Simon, E. Kirby, N. Ho, and A. Warres, Astron. J. **142**, 128 (2011), arXiv:1007.3499 [astro-ph.GA].

[48] M. Mateo, E. W. Olszewski, and M. G. Walker, Astrophys. J. **675**, 201 (2008), arXiv:0708.1327 [astro-ph].

[49] M. Ackermann *et al.* (Fermi-LAT Collaboration), Astrophys. J. Suppl. Ser. **203**, 4 (2012), arXiv:1206.1896 [astro-ph.IM].

[50] J. Bregeon *et al.* (Fermi-LAT Collaboration), (2013), arXiv:1304.5456 [astro-ph.HE].

[51] S. K. Portillo and D. P. Finkbeiner, Astrophys. J. **796**, 54 (2014), arXiv:1406.0507 [astro-ph.IM].

[52] J. Mattox, D. Bertsch, J. Chiang, B. Dingus, S. Digel, *et al.*, Astrophys. J. **461**, 396 (1996).

[53] W. A. Rolke, A. M. Lopez, and J. Conrad, Nucl.Instrum.Meth. **A551**, 493 (2005), arXiv:physics/0403059 [physics].

[54] H. Jeffreys, Proc. R. Soc. A **186**, 453 (1946).

[55] A. Burkert, Astrophys. J. **447**, 25 (1995), arXiv:astro-ph/9504041 [astro-ph].

[56] F. de Palma, T. Brandt, G. Johannesson, and L. Tibaldo (Fermi-LAT Collaboration), *2012 Fermi Symposium Proceedings*, eConf **C121028** (2013), arXiv:1304.1395 [astro-ph.HE].

[57] E. Carlson, D. Hooper, and T. Linden, (2014), arXiv:1409.1572 [astro-ph.HE].

[58] L. E. Strigari, S. M. Koushiappas, J. S. Bullock, M. Kaplinghat, J. D. Simon, *et al.*, Astrophys. J. **678**, 614 (2008), arXiv:0709.1510 [astro-ph].

[59] R. Essig, N. Sehgal, and L. E. Strigari, Phys. Rev. D **80**, 023506 (2009), arXiv:0902.4750 [hep-ph].

[60] W. Atwood *et al.* (Fermi-LAT Collaboration), Astrophys. J. **697**, 1071 (2009), arXiv:0902.1089 [astro-ph.IM].

[61] A. Charbonnier, C. Combet, M. Daniel, S. Funk, J. Hinton, *et al.*, Mon. Not. R. Astron. Soc. **418**, 1526 (2011), arXiv:1104.0412 [astro-ph.HE].

Supplemental Material: Searching for Dark Matter Annihilation from Milky Way Dwarf Spheroidal Galaxies with Six Years of Fermi-LAT Data

Pass 8 Event-Level Analysis

`Pass 8` is a new event-level analysis for the LAT instrument and is the successor to the `Pass 7 Reprocessed` event-level analysis [20, 49, 50]. Some of the key features of `Pass 8` are new algorithms to identify out-of-time signals, a new tree-based pattern recognition for the tracker subsystem, and an improved energy reconstruction that extends the LAT energy range below 100 MeV and above 1 TeV. `Pass 8` implements a new classification analysis based on boosted decision trees (BDTs), which provides enhanced background rejection power relative to `Pass 7 Reprocessed` [20]. The `Pass 8` event-level analysis enhances the capabilities of the LAT in all metrics relevant for high-level science analysis. In the energy range between 1 GeV and 10 GeV, the new P8R2_SOURCE event class has a 30–40% better point-source sensitivity than the P7REP_CLEAN event class.

`Pass 8` introduces an *event type* classification scheme that partitions events within a class according to their reconstruction quality. The event type classification is a generalization of the existing conversion type designation that identifies events converting in the *Front* or *Back* section of the tracker [51, 60]. `Pass 8` defines eight new event type selections based on a sequence of energy-dependent cuts on the BDT variables that categorize the quality of the direction and energy reconstruction. Four event types categorize the quality of the directional reconstruction (PSF0 to PSF3), and another four do so for the energy reconstruction (EDISP0 to EDISP3). By construction, these selections partition the gamma-ray acceptance at each energy such that an event class will have approximately the same number of events of each type.

Our maximum likelihood analysis of the dSphs combines the four P8R2_SOURCE_V6 PSF event types in a joint likelihood function. Although each event type contains approximately the same fraction of the total instrument acceptance, the angular resolution as measured by the 68% and 95% containment radii of the PSF is significantly better for events belonging to the best PSF event types. At 3.16 GeV the 68% (95%) containment radii of the acceptance-weighted PSF for the best and worst PSF event types (PSF3 and PSF0) is 0.17° (0.35°) and 0.92° (2.3°). By combining the event types in a joint likelihood function, we weight the contribution of events within a class by their reconstruction quality, e.g., events with the least well-characterized direction (PSF0) are assigned the lowest weight when testing the hypothesis of a putative DM source. We estimate that splitting the event sample by event type improves the sensitivity to an isolated point source by 10%. We expect that larger sensitivity gains will occur in regions where the gamma-ray intensity is strongly non-uniform.

Given these improvements, along with two additional years of data, our flux constraints are expected to improve by a factor of ∼1.7 below 10 GeV and ∼2.2 above 100 GeV relative to the analysis of Ackermann *et al.* [13]. Although both the `Pass 7 Reprocessed` and `Pass 8` analyses yield limits on the DM annihilation cross section within their respective 95% sensitivity bands, their constraints differ by a factor that is appreciably larger than expected from the median experimental sensitivities. For the $b\bar{b}$ channel, the `Pass 8` constraints are ~ 5 times lower at 100 GeV. For two independent data sets, statistical fluctuations can easily account for the difference in limit realizations.

We find that, at a given energy, only 20–40% of events in the six-year `Pass 8` SOURCE-class data set are shared with the four-year `Pass 7 Reprocessed` CLEAN-class data set. If the `Pass 8` SOURCE-class selection retains all events in the `Pass 7 Reprocessed` data set, we expect this fraction to equal the product of the ratio of gamma-ray acceptances for the two event classes with the ratio of observation times — in this case 35–50%. Since the basic event reconstruction in `Pass 8` is fundamentally different, however, the characteristics of individual events change slightly. Events near the threshold of any of our analysis cuts can migrate out of our data selection and be excluded from the `Pass 8` analysis. Specifically, 1–3% of the `Pass 7 Reprocessed` events were reconstructed outside of our ROIs, and 10–15% were not deemed likely enough to be photons to be included in the `Pass 8` SOURCE class. Figure 3 shows the fraction of shared events as a function of energy for the set of dSphs in our combined analysis, along with a sample of events from the Earth limb, selected from time periods when the magnitude of the rocking angle of the LAT was greater than 52°. The Earth's limb is an extremely pure photon source, and the fact that its shared fraction lies only slightly below the event class acceptance ratio indicates that the P8R2_SOURCE selection has a high efficiency for retaining gamma-ray events in the P7REP_CLEAN selection. The lower shared fraction observed in the dSph ROIs can be attributed to misclassified charged-particle events that constitute $\sim$ 30–40% of the diffuse, high-latitude background between 1 and 10 GeV. These events typically lie near the boundary of the selections used to discriminate gamma rays from charged-particle backgrounds and are much more likely to migrate out of a given event class than a true gamma-ray event.

Using the fractional overlap, we can estimate the evolution of a background fluctuation between analyses. For

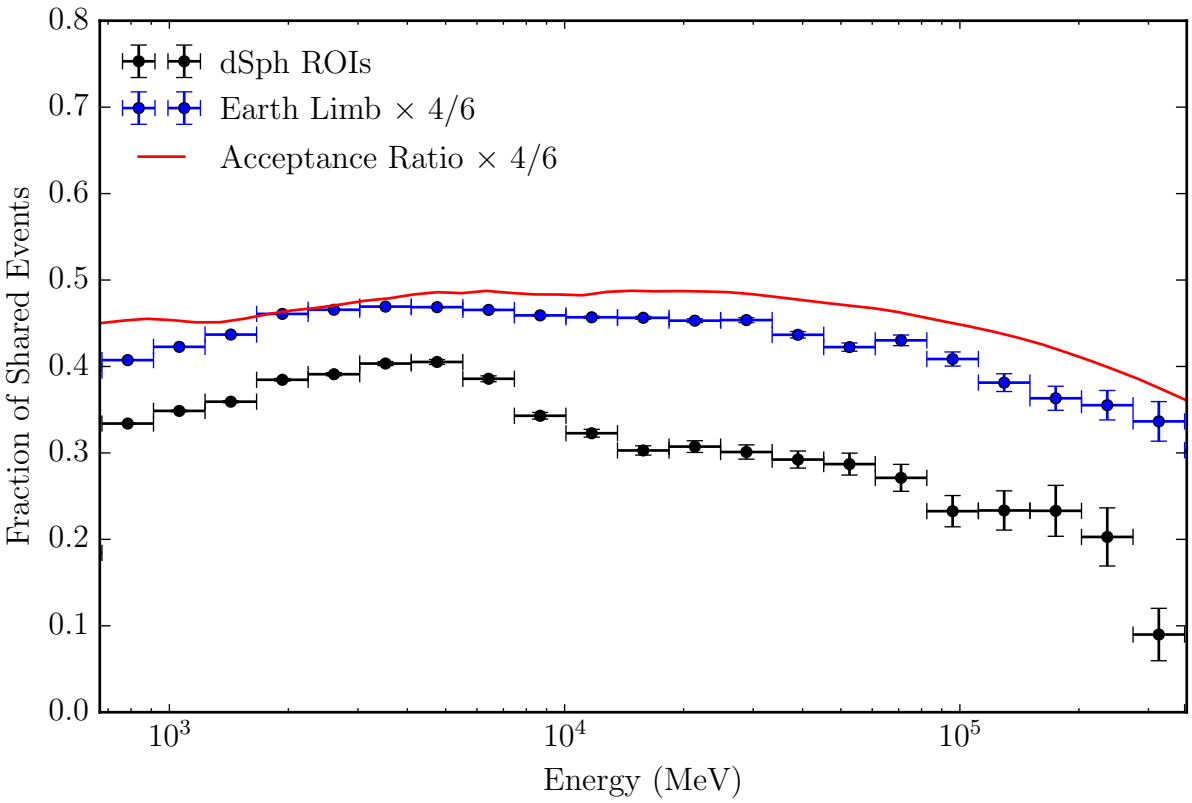

FIG. 3. Fraction of events in the 6-year `Pass 8` SOURCE data set that are also in the 4-year `Pass 7 Reprocessed` CLEAN data set. The lower points (black) show the shared fraction for events within 10° of one of the 15 dSphs used in the combined analysis. The upper points (blue) show the expectation for the shared fraction of a pure gamma-ray sample as derived from events taken from the Earth Limb. The red, solid line shows the acceptance ratio of P7REP_CLEAN_V15 to P8R2_SOURCE_V6 and represents the maximum possible shared event fraction. Both the Earth Limb fraction and acceptance ratios have been scaled by the ratio of the observation times of the 4- and 6-year analyses.

example, the largest `Pass 7 Reprocessed` excess occurred for the $b\bar{b}$ channel at masses between 10 and 25 GeV, and had a local significance of $\sim 3\sigma$. If we assume this excess resulted from an upward fluctuation of the background, the addition of new data is likely to reduce its significance. If the excess is due to a statistical fluctuation, we quantitatively expect the original significance, σ_1, to drop by a factor that depends only on the intrinsic fraction of shared events, f_i, and the ratio of observation times t_1/t_2,

$$\sigma_2 \approx \sigma_1 f_i \sqrt{t_1/t_2}, \tag{1}$$

where the intrinsic fraction is related to the observed fraction (f_{obs}) by $f_i \approx f_{obs}(t_2/t_1)$. In the energy range between 1 and 10 GeV, the `Pass 8` analysis shares f_{obs} ~35% of its events with `Pass 7 Reprocessed` and has a 50% longer observation period corresponding to an intrinsic shared fraction of f_i ~52%. A 3σ background fluctuation should therefore drop to $\sim 1.3\sigma$, which is consistent with our observations.

Galactic Diffuse Background Model

We model diffuse backgrounds in the dSph ROIs using templates that account for both astrophysical backgrounds and residual particle contamination. Our model for the Galactic diffuse emission is based on the `Pass 7 Reprocessed` diffuse emission model (`gll_iem_v05_rev1.fit`) that was derived from a fit to `Pass 7 Reprocessed` data with the P7REP_CLEAN_V15 IRFs. Although models of the Galactic diffuse emission are formally independent of the IRFs, the `Pass 7 Reprocessed` model was fit without accounting for energy dispersion which introduces some dependence on the `Pass 7 Reprocessed` IRFs. To create a model that can be used self-consistently with `Pass 8` data, we have

derived a rescaled model (`gll_iem_v06.fit`) that accounts for the influence of energy dispersion by correcting for the differences in apparent intensity in the `Pass 7 Reprocessed` and `Pass 8` data sets.

The correction for energy dispersion is derived from the ratio of the counts distributions computed with and without the correction for energy dispersion. Given an intensity, $I(E)$, the counts densities evaluated with energy dispersion (C_1) and assuming perfect energy resolution (C_2) are given by

$$C_1(E') = \int\int I(E) A_{\rm eff}(E,\theta) t_{\rm obs}(\theta) D(E';E,\theta) dE d\theta, \tag{2}$$

$$C_2(E') = I(E) \int\int A_{\rm eff}(E,\theta) t_{\rm obs}(\theta) \delta(E'-E) dE d\theta, \tag{3}$$

where E and E' are the true and measured energies, θ is the LAT incident angle ($\theta = 0$ is normal to the top of the LAT), $A_{\rm eff}(E,\theta)$ is the effective area, $t_{\rm obs}$ is the integrated livetime, and $D(E';E,\theta)$ is the energy dispersion. Defining ratios between the counts densities as $R_{P8} = C_1^{P8}/C_2^{P8}$ and $R_{P7REP} = C_1^{P7REP}/C_2^{P7REP}$, the rescaled model is $I_{P8}(E) = (R_{P8}/R_{P7REP}) I_{P7REP}(E)$. We note that the correction depends on the true intensity ($I(E)$) in Equations 2 and 3. We find that the correction is not strongly dependent on the assumed spectrum, and we use here the average all-sky intensity of the `Pass 7 Reprocessed` model. Systematic uncertainties associated with our model for the Galactic diffuse emission are discussed in more detail in the Systematic Uncertainties section.

Statistical Methodology

We use a maximum likelihood-based statistical formalism [52] to test the DM signal hypothesis and derive confidence intervals on $\langle\sigma v\rangle$. Our global likelihood function for $\langle\sigma v\rangle$ is constructed from the product of likelihood functions for individual dSphs in our sample. We compute the profile likelihood function as a function of $\langle\sigma v\rangle$ by maximizing the global likelihood function with respect to the nuisance parameters for each dSph ($\boldsymbol{\theta}_i = \{\boldsymbol{\alpha}_i, J_i\}$):

$$\lambda(\langle\sigma v\rangle, m_{\rm DM}) = \prod_i \tilde{\mathcal{L}}_i(\langle\sigma v\rangle, m_{\rm DM}, \hat{\boldsymbol{\alpha}}_i, \hat{\hat{J}}_i(\langle\sigma v\rangle, m_{\rm DM}) \,|\, \mathcal{D}_i). \tag{4}$$

Here, $\hat{\boldsymbol{\alpha}}_i$ are the best-fit parameters derived from a global fit with a free-normalization DM source with a $\Gamma = 2$ power-law spectrum and $\hat{\hat{J}}_i$ is the J-factor that maximizes $\tilde{\mathcal{L}}_i$ for a given $\langle\sigma v\rangle$ and $m_{\rm DM}$. Confidence intervals on $\langle\sigma v\rangle$ for a given $m_{\rm DM}$ are calculated with the delta-log-likelihood technique, requiring a change in the profile log-likelihood of 2.71/2 from its maximum for a 95% CL upper limit [53].

Among the nuisance parameters in Equation (4), we distinguish between parameters constrained by the gamma-ray data ($\boldsymbol{\alpha}$) and the J-factors (J), which are constrained by an independent analysis of stellar kinematics. We use J-factors derived from a two-level Bayesian hierarchical modeling analysis that incorporates information on both stellar kinematics and priors on the distribution of global dSph properties [8]. For each dSph the Bayesian analysis provides a posterior distribution function, $\mathcal{P}(J_i)$, which we approximate with a log-normal distribution with central value, $J_{\rm obs,i}$, and uncertainty, σ_i.

Following the approach developed in Ackermann *et al.* [10, 13], we account for statistical uncertainty on the J-factor by multiplying the LAT likelihood function with a J-factor likelihood function, $\mathcal{L}_J(J_i \,|\, J_{\rm obs,i}, \sigma_i)$. We construct an *ansatz* for the J-factor likelihood function by equating the sampling distribution of $J_{\rm obs,i}$ with $\mathcal{P}(J_i)$. With this underlying assumption, the likelihood function is given by a log-normal distribution with central value $J_{\rm obs,i}$ and width σ_i,

$$\mathcal{L}_J(J_i \,|\, J_{\rm obs,i}, \sigma_i) = \frac{1}{\ln(10) J_{\rm obs,i} \sqrt{2\pi}\sigma_i} e^{-(\log_{10}(J_i) - \log_{10}(J_{\rm obs,i}))^2/2\sigma_i^2}. \tag{5}$$

We note that Ackermann *et al.* [10, 13] used a different form for the J-factor likelihood function with $\mathcal{L}_J(J_i \,|\, J_{\rm obs,i}, \sigma_i) = \mathcal{P}(J_i)$ — i.e., a log-normal posterior. The J-factor likelihood function used in this work differs in the substitution of nominal J-factor ($J_{\rm obs,i}$) for the true J-factor (J_i) in the denominator of Equation (5). The log-normal likelihood formulation has several advantages over the log-normal posterior used in Ackermann *et al.* [10, 13]. When interpreted as a sampling distribution for $J_{\rm obs,i}$, it is properly normalized for all values of J_i. The maximum likelihood estimator $\hat{J}_i$ for the J-factor also coincides with its nominal value $J_{\rm obs,i}$ from the stellar kinematic analysis.

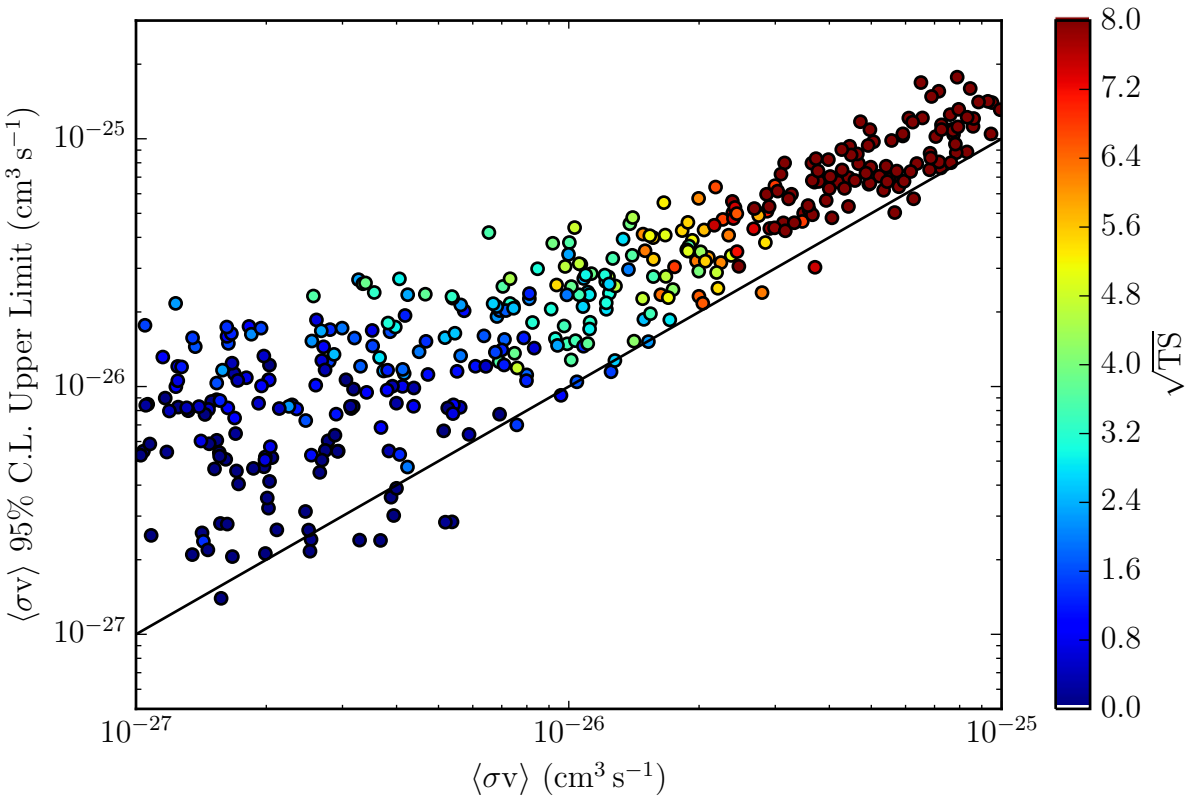

FIG. 4. Comparison of the 95% CL upper limit on $\langle\sigma v\rangle$ with its true value for a set of 400 MC realizations of the combined dSph analysis. In each realization a DM model with $m_{\mathrm{DM}} = 25$ GeV and a $b\bar{b}$ annihilation spectrum is injected at the locations of the dSphs using the set of nominal dSph J-factors. The DM cross-section is uniformly randomized in $\log\langle\sigma v\rangle$ between 10^{-27} and 10^{-25} $\mathrm{cm}^3\,\mathrm{s}^{-1}$. The measured J-factor ($J_{\mathrm{obs,i}}$) of each dSph is randomized by sampling from the J-factor posterior. The color of each point indicates the square root of the DM test statistic evaluated with the same spectrum as the injected DM model. Points above the solid diagonal line represent realizations where the upper limit covers the true value of the injected signal.

To confirm that our upper limits have the correct frequentist statistical coverage we have performed a series of independent Monte Carlo realizations of our analysis in which we include a DM signal. In these simulations the true J-factors are fixed to their nominal values while the measured J-factors are randomized by sampling from a log-normal approximation to the J-factor posterior of each dSph. Figure 4 shows the upper limits on $\langle\sigma v\rangle$ from one set of realizations simulated with a $b\bar{b}$ annihilation spectrum and $m_{\mathrm{DM}} = 25\,\mathrm{GeV}$. Under the assumption that the J-factor posterior is a good representation of the sampling distribution for J-factor measurements, we find that our statistical methodology produces the correct statistical coverage for a 95% CL upper limit.

Hybrid Bayesian Analysis

The main results of this work are evaluated with the delta-log-likelihood method, a fully frequentist statistical approach. In constructing the likelihood function of the delta-log-likelihood analysis, a central assumption is that the posterior distribution function is a good approximation to the J-factor sampling distribution. If this assumption holds, then our limits have the correct frequentist statistical coverage. To determine the robustness of our results to the choice of statistical methodology, we have performed an alternative analysis based on a Bayesian statistical approach in which we marginalize over the posterior distributions of the J-factors. For each target we use the same LAT likelihood function as for the primary analysis but set $\mathcal{L}_J = \mathcal{P}(J_i)$. We then marginalize over the J-factors to

derive a one-dimensional marginal posterior density,

$$\mathcal{P}(\langle\sigma v\rangle) = \frac{\int \prod_i \lambda_i(\langle\sigma v\rangle, m_{\rm DM}, J_i)\pi(\langle\sigma v\rangle)dJ_i}{\int \prod_i \lambda_i(\langle\sigma v\rangle', m_{\rm DM}, J_i')\pi(\langle\sigma v\rangle')d\langle\sigma v\rangle' dJ_i'}, \tag{6}$$

where $\pi(\langle\sigma v\rangle)$ is the prior for $\langle\sigma v\rangle$ and

$$\lambda_i(\langle\sigma v\rangle, m_{\rm DM}, J_i) = \mathcal{L}_i(\langle\sigma v\rangle, m_{\rm DM}, J_i, \hat{\boldsymbol{\alpha}}_i) \times \mathcal{P}(J_i) \tag{7}$$

is the product of the likelihood for target i with its J-factor posterior. Given the marginal posterior density of Equation (6), we derive an upper limit by finding the value $\langle\sigma v\rangle_0$ that satisfies $\int_{\langle\sigma v\rangle_0}^{\infty} \mathcal{P}(\langle\sigma v\rangle)d\langle\sigma v\rangle = p$ where we use $p = 0.05$ to define a Bayesian equivalent to the frequentist 95% CL upper limit.

An important consideration for the Bayesian analysis is the choice of the prior distribution, $\pi(\langle\sigma v\rangle)$, which is needed to evaluate the posterior density in Equation (6). In order to choose a prior that minimally influences our inference on $\langle\sigma v\rangle$, we consider the class of non-informative priors derived according to Jeffreys' rule [54]. As two approximations to the Jeffreys' prior for our likelihood, we take the Jeffreys' prior for the mean of a Gaussian distribution of known width, the uniform prior with $\pi(\mu) = 1$, and the Jeffreys prior for a Poisson distribution, $\pi(\mu) = \mu^{-1/2}$, which we refer to here as the Poisson prior. The uniform prior should be applicable when the expected background is large relative to the signal and the LAT sensitivity is background-limited. In this regime the likelihood function of the LAT data given the model asymptotically approaches a Gaussian distribution. On the other hand, the Poisson prior is applicable when the expected background is negligible and the likelihood is well approximated by a Poisson distribution. For spectral models of WIMP annihilation through quark or lepton channels, the background- and signal-limited sensitivity regimes correspond to models of low and high mass, respectively.

Figure 5 compares limits for the $b\bar{b}$ channel calculated with the delta-log-likelihood and Bayesian analyses. In this comparison we calculate two sets of Bayesian upper limits using the $\langle\sigma v\rangle$ marginal posterior (Equation 6) and substituting the uniform and Poisson priors for $\pi(\langle\sigma v\rangle)$. We find that the Bayesian upper limits are in good agreement with the limits of the delta-log-likelihood analysis when the appropriate prior is chosen for the form of the likelihood on $\langle\sigma v\rangle$. For DM masses below 100 GeV where the likelihood is well approximated by a Gaussian, the limits from the Bayesian analysis with a uniform prior lie within 10% of those from the delta-log-likelihood analysis. At higher DM masses, a similar level of agreement (10–20%) is observed when comparing the delta-log-likelihood limits to the limits evaluated with the Poisson prior. We note that these changes are comparable to or smaller than the effect of the systematic uncertainties considered in the following sections. We conclude that our upper limits are robust to the choice of statistical methodology used to model the J-factor uncertainties.

Systematic Uncertainties

The dominant systematic uncertainties of this analysis arise from incomplete knowledge in three areas: the LAT instrument response, the Galactic diffuse gamma-ray background, and the distribution of DM in the dSphs. To estimate the impact of these uncertainties, we repeat our DM search using varying assumptions intended to encompass the range of possibilities in each of these areas. Below we address systematics associated with the IRFs and diffuse background model, which both affect constraints at the 10% level, with the latter becoming less relevant for hard DM spectra ($m_{\rm DM} > 100\,{\rm GeV}$). Systematics associated with the J-factors are addressed in the following section, while here we quote the maximum deviation from our fiducial NFW model, which occurs when assuming a cored Burkert density profile [55],

$$\rho_{\rm DM}(r) = \frac{\rho_0 r_s^3}{(r_s + r)(r_s^2 + r^2)}. \tag{8}$$

The J-factor systematic uncertainty has a greater impact than that of the IRF or diffuse models, approximately 35% at 100 GeV. We provide a summary of the systematic uncertainty as a function of DM mass and annihilation channel in Table II.

In addition to the standard model of interstellar gamma-ray emission for the LAT, we consider eight alternative models to sample a fairly wide range of possibilities for the diffuse gamma-ray background [56]. Although we can vary parameters *within* our background models, there are no doubt sources of gamma-ray emission that remain unmodeled. It was observed by Ackermann *et al.* [13] that the TS distribution from random blank sky locations deviated from statistical expectations, suggesting an incomplete background model. This indicated that a rescaling

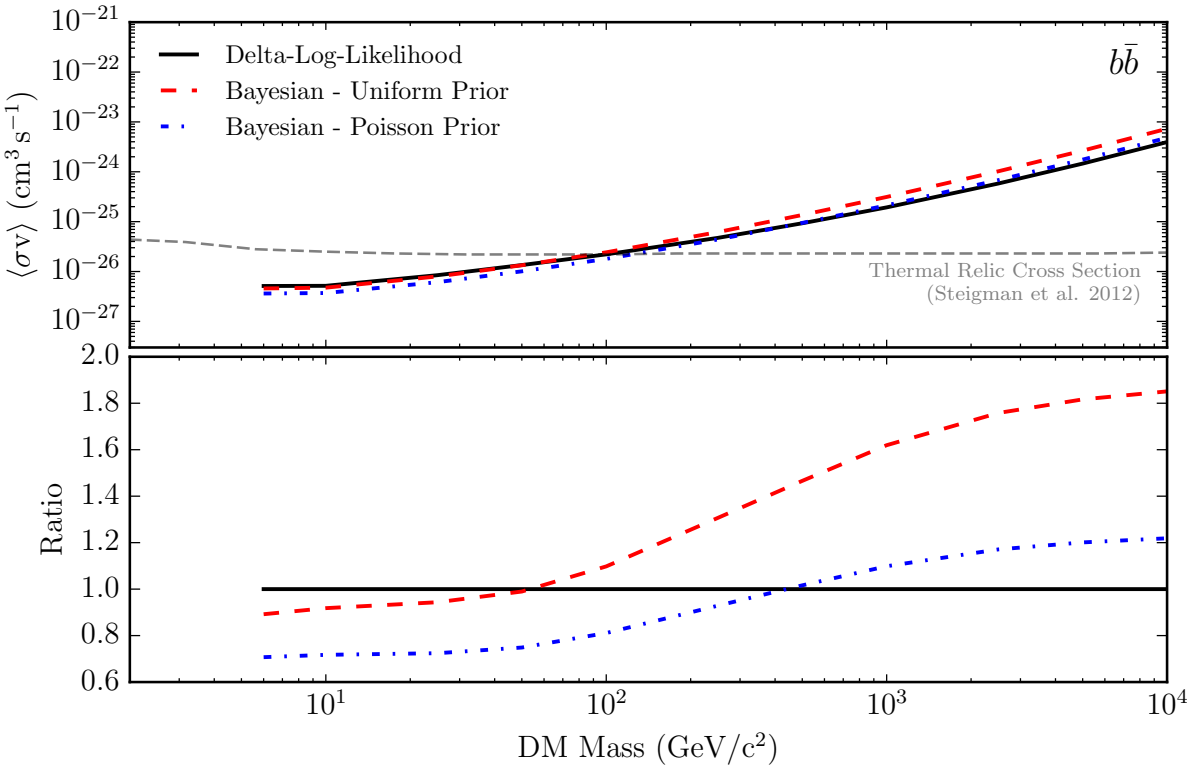

FIG. 5. Comparison of upper limits ($b\bar{b}$ channel) for the combined analysis of 15 dSphs as derived with the delta-log-likelihood analysis (solid line) and the Bayesian analysis performed with a uniform (dashed line) and Poisson (dot-dashed line) prior. The lower panel shows the ratio of these curves to the limits for the delta-log-likelihood analysis.

was necessary when converting from TS to significance, effectively lowering the sensitivity of the study. One large class of objects known to be unmodeled are sub-threshold point sources, i.e., those which contribute gamma rays but are not significant enough individually to be included in a catalog. It has been speculated that these give rise to the larger than expected rate of type I errors (false positives) that skew the TS distribution relative to the expectation from Poisson statistics [13, 57].

Figure 6 shows the distribution of TS obtained from the analysis of randomized ROIs when the data are analyzed using the 2FGL and 3FGL catalogs. We additionally analyze simulated ROIs with the 3FGL catalog using an input model for the simulations that includes 3FGL sources and our templates for the Galactic and isotropic diffuse backgrounds. Using the 3FGL, which roughly doubles the number of modeled sources, brings the TS distribution closer to the asymptotic expectation. However, a significant deviation with respect to the asymptotic expectation from Chernoff's theorem is still observed, indicating that additional unmodeled components may still be present in the data.

The uncertainty in the LAT response is bracketed by using IRFs that are maximally and minimally sensitive to our signal. The maximally sensitive set has a greater effective area, narrower PSF, and accounts for dispersion in the reconstructed energy. The minimally sensitive IRFs are the opposite. The effective area is set at the boundaries of the envelope described in Ackermann *et al.* [49], while the energy dispersion and PSF width are scaled by ±5% and ±15%, respectively.

J-factor Uncertainties

We have described a statistical methodology to account for uncertainties on the J-factors when deriving limits on the DM annihilation cross section. This procedure captures statistical uncertainties on the J-factor arising from the analysis of stellar velocity dispersion data. As implemented in the likelihood, it is not intended to account for additional systematic uncertainties. Such systematic uncertainties on the J-factor include parameterization of the

TABLE II. Effect of systematic uncertainties for various WIMP masses and channels reported as a symmetrical relative deviation from the combined 95% CL upper limits.

		10 GeV	100 GeV	1 TeV	10 TeV
e^+e^-	IRFs	6%	10%	11%	11%
	Diffuse	12%	6%	3%	2%
	J-factor	29%	31%	17%	16%
$\mu^+\mu^-$	IRFs	6%	10%	11%	11%
	Diffuse	13%	6%	3%	2%
	J-factor	28%	32%	18%	16%
$\tau^+\tau^-$	IRFs	7%	9%	11%	11%
	Diffuse	15%	6%	1%	1%
	J-factor	24%	35%	15%	14%
$u\bar{u}$	IRFs	6%	7%	9%	10%
	Diffuse	23%	12%	7%	4%
	J-factor	16%	34%	31%	24%
$b\bar{b}$	IRFs	6%	7%	9%	11%
	Diffuse	23%	13%	7%	4%
	J-factor	13%	32%	32%	23%
W^+W^-	IRFs		7%	10%	11%
	Diffuse		13%	6%	2%
	J-factor		32%	31%	17%

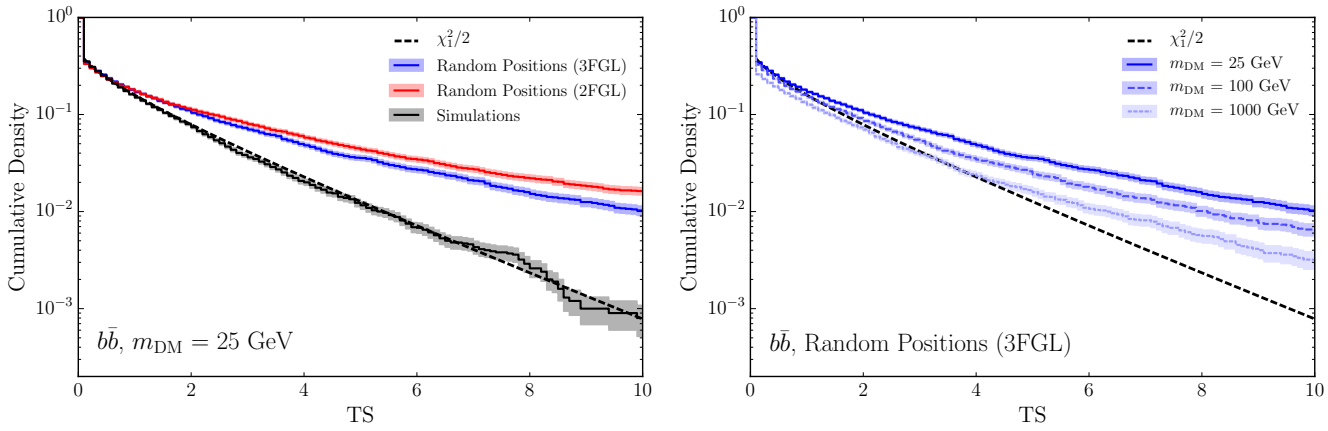

FIG. 6. Cumulative distribution of TS from 7500 randomized blank-sky regions fit with a DM particle annihilating through the $b\bar{b}$ channel. Shaded bands indicate the one sigma uncertainties on the cumulative fraction, which are highly correlated between bins. *Left panel:* Distributions for a DM mass of 25 GeV evaluated from Monte Carlo simulations (black line) and LAT data analyzed with the 3FGL (blue line) and 2FGL (red line) point-source catalogs. *Right panel:* Distributions for DM masses of 25 GeV, 100 GeV, and 1000 GeV evaluated with LAT data analyzed with the 3FGL point-source catalog. As illustrated by this plot, the TS distribution depends on the parameters of the WIMP spectral model (annihilation channel and mass). Harder spectral models (e.g., those with higher mass) have a distribution that lies closer to the asymptotic expectation from Chernoff's theorem.

DM profile and the choice of priors for the profile parameters. While previous studies have shown that the derived J-factors are robust against these systematic uncertainties for dSphs with large stellar data sets [58], it is nonetheless important to quantify their impact. To assess the impact of systematic uncertainties in the J-factor derivations, we examine a set of four alternative J-factors derived by various fitting methods.

The first set of alternative J-factors comes from the recent analysis of Geringer-Sameth *et al.* [9] assuming a generalized NFW profile with non-informative priors on its parameters. We also examine the J-factors derived by Charbonnier *et al.* [61] assuming a generalized Hernquist profile with uniform priors. Additionally, we perform our own alternative analysis following the procedure of Essig *et al.* [59] assuming a simple NFW profile with non-informative priors on the scale radius and scale density, and a velocity anisotropy parameter that is assumed to be constant with radius. Lastly, we show results derived from the multi-level modeling approach of Martinez [8] assuming a cored Burkert profile as presented in Ackermann *et al.* [13].

For each of these alternative sets of J-factors, we re-derive the limit on the DM annihilation cross section in the context of the LAT data. For cuspy spatial profiles, the spatial template of the DM distribution has little impact on the LAT analysis. Thus, for the first three sets of alternative J-factors we only alter the nominal J-factor and associated uncertainty. When assuming a Burkert profile, we use the full spatial profile of the assumed DM distribution (the change in spatial profile affects the limits by $< 5\%$). Since the analyses of Charbonnier *et al.* [61] and Geringer-Sameth *et al.* [9] do not include all of the dwarfs used in our analysis, when a dSph is missing from one of these data sets we assign it the nominal J-factor and uncertainty from Table I in the main text. When asymmetric errors are given for the best-fit J-factor, we use the geometric mean to set the width of the log-normal J-factor likelihood.

The resulting change in the upper limit on the DM cross section is shown in Figure 7. The mass dependence of the curves in Figure 7 reflects the fact that by changing the J-factors we change the relative importance of each dSph, leading to an interplay between the LAT data and the assumed J-factors. Unsurprisingly, the largest change in the upper limit comes from requiring a cored Burkert profile. This increases the upper limit by a factor of 20–40% with respect to the nominal limit (this is slightly larger than was observed by Ackermann *et al.* [13]) and is what we quote in Table II as the overall J-factor systematic uncertainty. The J-factors derived by Charbonnier *et al.* [61] and the alternative analysis with non-informative priors both yield slightly smaller changes in the limit. Finally, we observe that the J-factors from Geringer-Sameth *et al.* [9] are most similar to the nominal J-factors and result in differences of 5–10%.

The combined limits presented here include both classical and ultra-faint dSphs. Bayesian hierarchical modeling sets rather tight constraints on the J-factors of the ultra-faint dSphs as members of the dSph population; however, stellar kinematic data yield larger uncertainties on ultra-faint dSphs when analyzed individually. To assess the maximum impact of mis-modeling the ultra-faint dSphs, we split the dSph population into ultra-faint (Bootes I, Canes Venatici II, Coma Berenices, Hercules, Leo IV, Segue 1, Ursa Major II, Willman 1) and classical (Carina, Draco, Fornax, Leo II, Sculptor, Sextans, Ursa Minor) galaxies. For soft annihilation spectra (e.g., the $b\bar{b}$ channel for DM with mass $< 100\,\mathrm{GeV}$), the classical and ultra-faint populations yield comparable limits, each $\sim 40\%$ worse than the combined limit. For harder annihilation spectra with spectral energy distributions that peak above 10 GeV, the limits from the ultra-faint population are roughly comparable to the combined limits, while the classical dSphs yield limits up to five times weaker. Considering only the classical dSphs, models with the thermal relic cross section are excluded for slightly lower masses ($\lesssim 80\,\mathrm{GeV}$).

Annihilation Channels

WIMPs may annihilate through a variety of Standard Model channels. For the quark and boson channels, the resulting gamma-ray spectra are all similar and largely depend on m_{DM}. The three leptonic channels have harder spectral energy distributions with a peak in energy flux that is closer to m_{DM}. We perform our analysis for six representative annihilation channels ($b\bar{b}$, $\tau^+\tau^-$, $\mu^+\mu^-$, e^+e^-, W^+W^-, and $u\bar{u}$) and for each we assume a 100% branching fraction. The resulting constraints, shown in Figure 8, are similar to the $b\bar{b}$ and $\tau^+\tau^-$ channels depicted in the main body of this work, except for the e^+e^- and $\mu^+\mu^-$ channels which are somewhat higher.

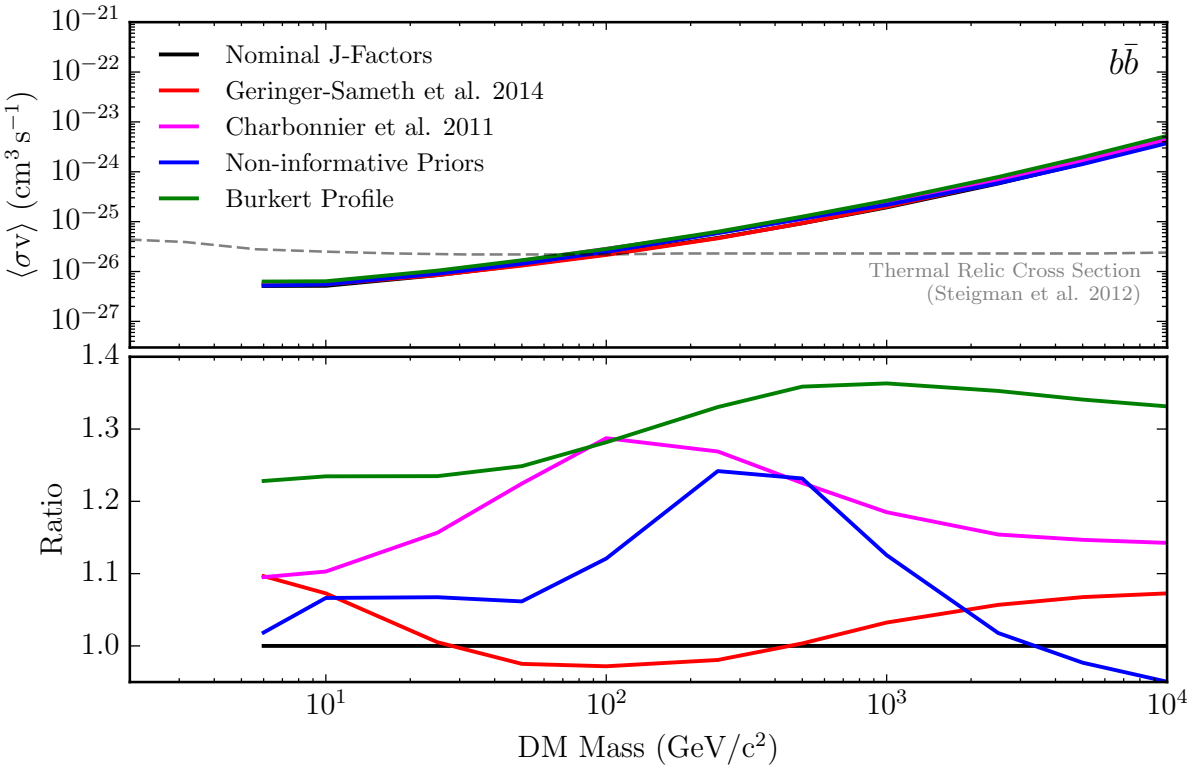

FIG. 7. Change in the limits derived for the DM annihilation cross section under the assumption of alternative sets of J-factors. Alternative J-factors are taken from Geringer-Sameth *et al.* [9] and Charbonnier *et al.* [61]. Non-informative priors are used to derive J-factors following the procedure of Essig *et al.* [59]. Burkert J-factors are derived using the multi-level modeling approach of Martinez [8] and are taken from Ackermann *et al.* [13].

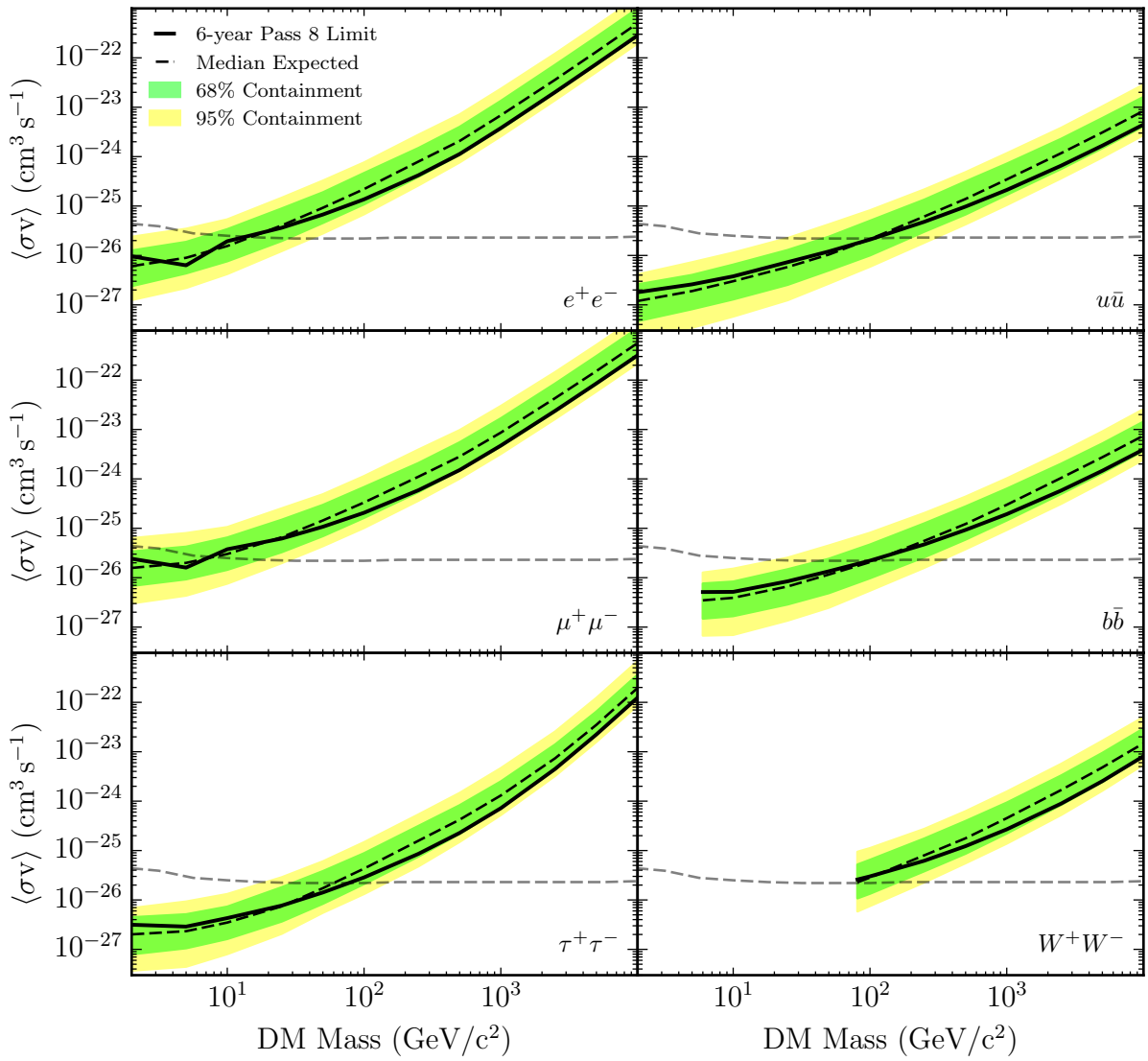

FIG. 8. DM annihilation cross-section constraints derived from the combined 15-dSph analysis for various channels.